

Integrating plasmonic diagnostics and microfluidics

Lifang Niu,¹ Nan Zhang,¹ Hong Liu,¹ Xiaodong Zhou,¹ and
Wolfgang Knoll^{1,2,3}

¹*Institute of Materials Research and Engineering, 3 Research Link, Singapore 117602, Singapore*

²*Center for Biomimetic Sensor Science, Nanyang Drive 50, Singapore 637553, Singapore*

³*AIT Austrian Institute of Technology, Muthgasse 11, 1190 Vienna, Austria*

(Received 28 May 2015; accepted 13 August 2015; published online 2 September 2015)

Plasmonics is generally divided into two categories: surface plasmon resonance (SPR) of electromagnetic modes propagating along a (noble) metal/dielectric interface and localized SPRs (LSPRs) on nanoscopic metallic structures (particles, rods, shells, holes, etc.). Both optical transducer concepts can be combined with and integrated in microfluidic devices for biomolecular analyte detections, with the benefits of small foot-print for point-of-care detection, low-cost for one-time disposal, and ease of being integrated into an array format. The key technologies in such integration include the plasmonic chip, microfluidic channel fabrication, surface bio-functionalization, and selection of the detection scheme, which are selected according to the specifics of the targeting analytes. This paper demonstrates a few examples of the many versions of how to combine plasmonics and integrated microfluidics, using different plasmonic generation mechanisms for different analyte detections. One example is a DNA sensor array using a gold film as substrate and surface plasmon fluorescence spectroscopy and microscopy as the transduction method. This is then compared to grating-coupled SPR for poly(ethylene glycol) thiol interaction detected by angle interrogation, gold nanohole based LSPR chip for biotin-streptavidin detection by wavelength shift, and gold nanoholes/nanopillars for the detection of prostate specific antigen by quantum dot labels excited by the LSPR. Our experimental results exemplified that the plasmonic integrated microfluidics is a promising tool for understanding the biomolecular interactions and molecular recognition process as well as biosensing, especially for on-site or point-of-care diagnostics.

© 2015 AIP Publishing LLC. [<http://dx.doi.org/10.1063/1.4929579>]

I. INTRODUCTION

Biomolecular interactions and molecular recognition processes are important to understand in order to gain a deeper insight into biological phenomena such as immunologic reactions or signal transduction. In addition, these biological recognition reactions have been proposed to be used in biosensor applications. A number of sensing/transduction methods have been developed over the past years that are now used in biology, medicine, and pharmacy. Novel detection principles have been demonstrated which combine the specificity of biomolecular recognition systems with the advantages of instrumental analysis.

There are several challenges in the field of design, assembly, and characterization of supramolecular (bio-) functional interfacial architectures for optical biosensing applications. The first is the development of immobilization technologies for stabilizing biomolecules and tethering them to a surfaces.¹ The usual aim is to produce a thin film of immobilized biologically active material at or near the transducer surface which responds only to the presence of one or a group of materials or substances of interest. Since the immobilization technique used to attach the biological material to the sensor surface is crucial to the operational behavior of the biosensor, optimized strategies for the development of immobilization techniques are essential for practically useful biosensors.

The other important challenge is to develop detection techniques that have the potential for highly controlled on-line monitoring of the interaction activities and binding events. Only a combination of a variety of techniques can lead to the full understanding of the complex processes occurring at the sensor surface. In particular, techniques based on different transducer principles can be combined to test the underlying assumptions used for the interpretation of the response, and provide more detailed information about the system of interest.

This report deals first with the development of a sensor array strategy based on the electrochemical control of the functionalization, in order to fabricate biosensor arrays with supramolecular interfacial architectures in a micro-fluidic environment.

Part of the corresponding study also focused on the realization of parallel detection of the processes taking place on each individual sensor element of a whole microarray by Surface Plasmon Microscopy (SPM) and the parallel detection of hybridization reactions at the array surface by Surface Plasmon Field-Enhanced Fluorescence Microscopy (SPFM).

Section III deals with the excitation of surface plasmons by grating couplers as an integral part of the microfluidic channel thus allowing for a higher integration of the fluidic chip features and the detection units.

And finally, we present concepts for the integration of Au-nanostructures, used for the excitation of localized surface-plasmon modes and for the enhanced detection of bio-affinity reactions at the surface of the microfluidic channels.

For the combination of the plasmonics with microfluidics, there are some recent reviews published.²⁻⁵ However, we see our paper not as a review, rather it is a summary report on our own work on combinations of microfluidics with various surface plasmon optical detection principles and a focus on applications for point-of-care systems.

II. *IN-SITU* MONITORING OF THE INTERFACE BY SURFACE-PLASMON OPTICAL TECHNIQUES

For the assay development in the format of a micro array, there is a need for rapid, multiple, and reliable analytical approaches for the detection of binding events between the immobilized ligands and specific biomolecules from solution. Surface plasmon resonance (SPR) spectroscopy has become widely used in the fields of chemistry and biochemistry for the characterization of biological surfaces to monitor such binding events.⁶ The use of plasmon surface polaritons as interfacial light has been discussed in the literature in great detail and hence will be outlined only very briefly.

In the so-called Kretschmann configuration (see Fig. 1(a)), the nearly free electron gas in the thin (~ 50 nm) noble metal film evaporated onto the base of the prism acts as an oscillator that can be driven by the electromagnetic wave impinging upon that interface at total internal reflection conditions. This resonance phenomenon can be clearly seen in the attenuated total reflection (ATR) scan (see Fig. 1(c)). Below the critical angle, θ_c , the reflectivity is very high because the metal film acts as a mirror with little transmission. Above θ_c for total internal reflection, however, a relatively narrow dip in the reflectivity curve indicates the resonant excitation of such a surface plasmon polariton (SPP) wave propagating at the metal/dielectric interface. The coupling angle is given by the energy- and momentum-matching condition between photon and surface plasmon,

$$k_{sp} = k_{ph}^0 = n_1 \left(\frac{\omega}{c} \right) \sin \theta, \quad (1)$$

with k_{ph}^0 being the parallel component of the photon wave vector, ω is the photon energy, c is the speed of light, and θ is the (internal) coupling angle (cf. Figs. 1(a) and 1(b)).

A thin dielectric coating causes a shift of the dispersion curve to higher momentum which, in turn, shifts the resonance to a higher angle (cf. Fig. 1(c)). From this shift and Fresnel's equations, one can calculate the optical thickness of the coating.⁷ If the formation of such a thin coating is observed on-line, e.g., during an adsorption process of proteins from solution to the solid/liquid interface, by monitoring the reflected intensity at a fixed angle of observation (see

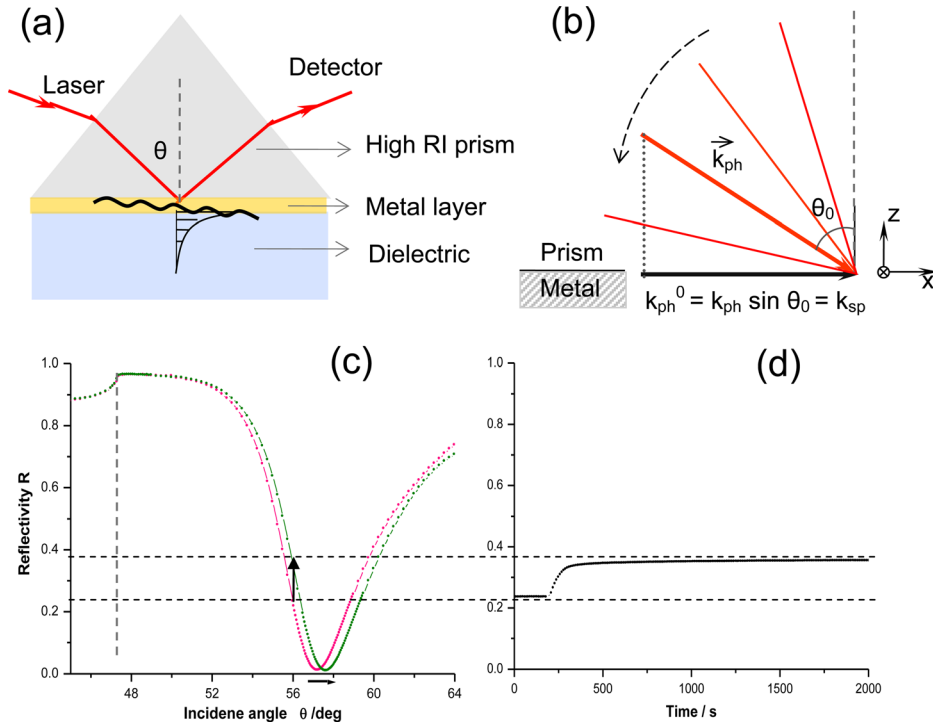


FIG. 1. (a) Kretschmann geometry for the excitation of surface plasmons. A thin metal film is evaporated onto the base of a glass prism and acts as a resonator driven by the photon field. (b) The momentum of the incident light beam in the plane of the interface exceeds the one needed for the SPP excitation. Thus, at the incident angle of θ_0 , where the energy and the x-component of the momentum are matched between photons and surface plasmons, a SPP mode is excited. (c) The resonant excitation of surface plasmons is seen in the reflectivity curve as a sharp dip at θ_0 (red curve) which shifts upon the deposition of a thin film (green curve). (d) Kinetic information, e.g., on this time-dependent layer formation can be obtained by monitoring the reflected intensity at a fixed angle of observation.

Fig. 1(d)), kinetic information about the diffusional transport of mass to the interface, or the association and dissociation rate constants describing the binding process can be obtained.⁸

It is straightforward to extend SPR's applicability for multiplex detections by converting an SPR setup (cf. Fig. 2(a)) to a microscope via addition of an imaging lens in the reflected light and a CCD camera on the detection side so as to obtain images of the interface with a contrast

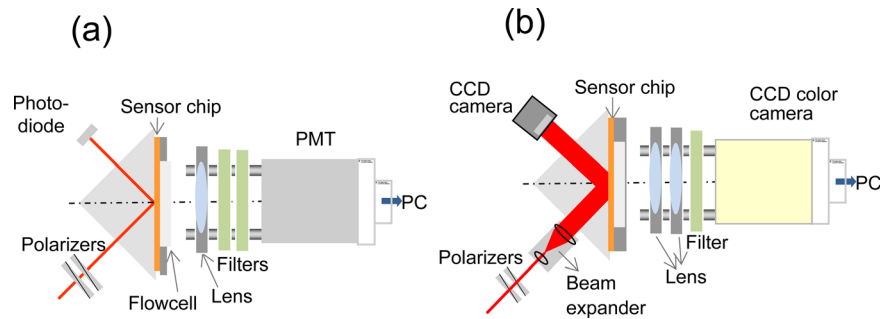


FIG. 2. Schematic diagram of surface plasmon spectroscopic and microscopic configurations. (a) Upgraded spectroscopic versions include conventional SPR and SPFS (surface plasmon field-enhanced fluorescence spectroscopy) measurement units. While the photo-diode detects the reflected light at 2θ , the photomultiplier and photo-counter unit are mounted towards the base of the prism, rotating together with the prism (sample) at θ . The fluorescence emission from the sample surface is collected by a lens, directed by band-pass and interference filters into the PMT tube. (b) Upgraded microscopic versions include an SPM (surface plasmon microscope) and SPFM (surface plasmon field-enhanced fluorescence microscopy). An expanded beam is reflected from chip surface and then imaged onto a monochromatic CCD camera. The CCD camera is connected to a frame-grabber card for image transmitting. Another particularly sensitive color CCD camera is attached normal to the substrate surface for the recording of the fluorescence images.

that originates from either lateral thickness or refractive index variations.⁹ The flow cell is a simple channel with inlet and outlet with tubes to manage the analyte liquid. It can be fabricated by hot embossing of plastic chips for microsize feature channels, or fabricated by mechanical machining for critical feature above 200 μm . The operation of the so-called SPM is completely equivalent to the procedure in any other microscopy except that the sample is “illuminated” with surface bound light rather than with “normal” photons or electrons. A schematic of the corresponding setup is given in Fig. 2(b).¹⁰ The video signal of the camera is digitized by a frame grabber unit and the captured images can be quantitatively analyzed by a computer. With a typical frame transfer time of ca. 20 ms, kinetic property changes or processes at the interface or in thin films can be easily followed at that time resolution. It can be shown that this microscopic mode of surface-plasmon optics allows for the recording of only subtle thickness changes of a few tenths of a nanometer.

Further efforts to enhance the sensitivity of the SPR technique have been made especially by combining SPP resonance with fluorescence labeling.¹¹ The resonant excitation of an evanescent SPP mode can be used to excite the fluorophores chemically attached to the analyte molecules. Upon binding to the receptor at the metal/solution interface, the fluorophore reaches the strong SPP optical fields and gets excited. The emitted fluorescence photons are collected and analyzed in the usual way to give information about the behavior of the analyte itself. The use of fluorescence detection schemes in combination with the resonant excitation of surface plasmon has been shown to increase the sensitivity for bioanalyte monitoring considerably.¹²

The fluorescence detection unit (see Figs. 2(a) and 2(b)) is mounted towards the base of the prism, rotating together with the prism (sample) at θ , while the photo-diode detecting the reflected light rotates at 2θ . The fluorescence emission from the sample surface is collected by a lens into a photomultiplier tube (PMT) and a photo-counter unit (cf. Fig. 2(a)). This conformation is called surface Plasmon Field-Enhanced Fluorescence Spectroscopy (SPFS). Similarly, if the photomultiplier and photo-counter unit are replaced with a particularly sensitive color CCD camera, the fluorescence emission can be collected and imaged in order to gain applicability for multiplex detection. This detection configuration was introduced as Surface Plasmon Field-Enhanced Fluorescence Microscopy (SPFM).¹³

III. THE CONCEPT OF ELECTROCHEMICAL PATTERNING

Patterning of microscopic arrays for multiple chemical screening and biological analysis has been a central effort in sensor development for many years. Quite a few patterning methods have been developed and commonly used, such as microwriting,¹⁴ microstamping,¹⁵ and micro-machining.¹⁶ We describe here another strategy which utilizes addressable electrochemical control of the sensing elements to fabricate sensor arrays with a variety of supramolecular interfacial architecture. Our interests in developing this patterning strategy originates from the need to develop methods amenable to fabricate (DNA- and protein-) arrays for parallel analysis in a micro-fluidic platform without experiencing problems associated with multiple mask alignments and/or loss of biological activity encountered with ex-situ techniques.

The basis of this array strategy originates from the electrochemical control of the *in situ* assembly and disassembly (desorption) of thiol SAMs on gold surfaces. The electrochemical desorption of thiol monolayers from gold surfaces has been introduced¹⁷ and used for the patterning of SAMs via phase-separated binary monolayers,¹⁸ by STM tip-induced lithography¹⁹ and in micro-arrays of gold electrodes.²⁰ The incorporation of a wide variety of groups both in the alkyl chain and at the chain terminus of the thiol derivatives, and their use as building blocks allow for the fabrication of (laterally patterned) supramolecular interfacial architectures. For example, gold electrodes modified by thiolated DNA have been proven to be useful platforms in both the study of fundamental questions as well as for the application of DNA mediated charge transport (CT)²¹ with the electrochemical detection being highly sensitivity and relatively inexpensive.²²

After a systematic study of the electrochemical desorption of thiol monolayers from gold electrodes, we fabricated a patterned gold surface in a micro-fluidic device, i.e., an array of

gold electrode stripes each of which works independently both as an electrode and as a specifically functionalized sensing element. For simplicity, we present here a study of the fabrication and performance characterization of a 4-element addressable sensor system. Thiol-terminated methoxy polyethylene glycol (PEG-thiols) was first assembled to form a hydrophilic protecting monolayer on all gold stripes. Electrochemical desorption of the PEG-thiol from only one of those electrodes resulted in a bare gold surface on this particular stripe available for further functionalization. A sequence of thiolated biotin, streptavidin, and biotinylated oligonucleotide strand solutions were then applied to this bare gold electrode to eventually functionalize this sensor element with the desired capture probe sequence. The other electrodes were then subject to the same electrochemical desorption and step-by-step build-up procedures until finally all electrodes were labeled with different probe oligonucleotides except one which worked as an inert reference control for the DNA hybridization analysis. The whole preparation was performed in aqueous solution minimizing the risks of losing the molecules' bioactivity.

It should be noted that the total thickness of all these bio-functional building blocks on the gold electrodes adds up to only a few nanometers. However, by employing Surface Plasmon Microscopy^{23,24} one can document the interfacial build-up visually in real time and can gain quantitative information about the binding reactions.

In the work presented here, the SPFM was then used to quantify the parallel detection of hybridization reactions taking place at the whole microarray of individual sensor spots by using a highly sensitive color CCD camera as the recording element. The camera took images of the fluorescence intensities emitted from each sensor element arranged on the chip surface. This way, a large number of individually functionalized spots could be monitored simultaneously. For simplicity, we focus here on a study of an array of 4 spots of three different probe oligonucleotide sequences and their mixtures.

IV. ELECTROCHEMICAL DESORPTION OF PEG THIOLS BY POTENTIAL SWITCHING

SAMs terminated with PEG have been well-studied and found to generate among the most inert surfaces. We chose to study PEG thiol SAMs also because it has been indicated from previous research that inert PEG SAMs tend to have overall electrically neutral surfaces.^{25,26}

The adsorption and the irreversible reductive desorption of the (buffer soluble) PEG thiol (MW ~ 5 k) from the Au substrate was monitored by SPR kinetic measurements in a flow cell with HeNe laser excitation at $\lambda = 632.8$ nm; the results are given in Fig. 3. The potential applied to the bare gold substrate was cycled 3 times between $E = 0$ V and $E = -1.1$ V. The observed rapid decrease in reflectivity upon applying $E = -1.1$ V is attributed to changes in the electron

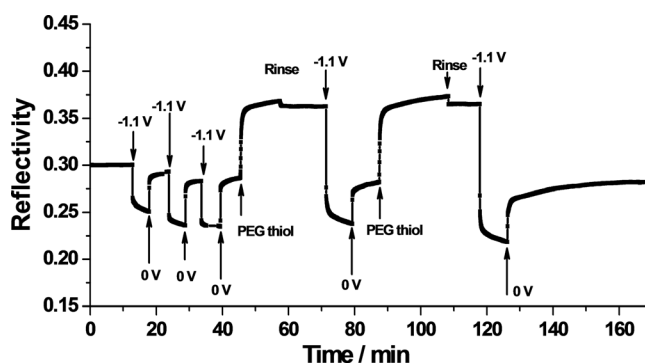


FIG. 3. Repetitive adsorption and electrochemical desorption processes of PEG thiols on the Au electrode at various applied potentials, as recorded by an SPR kinetic measurement. First, the potential of -1.1 V was loaded and released on bare gold substrate for three cycles. The reflectivity curve returns to the initial value, indicating that no major adsorption to or desorption from this bare gold surface happened. Next, the introduction of an aqueous PEG thiol solution results in a fast self-assembling process to the Au surface followed by quick saturation. The loading of a potential of $E = -1.1$ V potential causes a great reflectivity decrease so that upon releasing it to 0 V, the reflectivity reaches again the value of bare Au, indicating the reductive desorption of the PEG thiol SAM from gold surface. Repeated adsorption/desorption cycles give the same result.

density²⁷ at the metal/solution interface as well as refractive index changes of the dielectric medium close to the Au substrate caused by the potential-induced ion redistribution. Kötzt *et al.* had observed that the reflectance minimum of the SPR red-shifted upon applying a positive potential. Because surface and volume plasma frequencies are proportional to the square root of the free electron density, and the electron density at the interface can be reduced significantly by the positive potential. Once the potential was reset to $E=0$ V, the reflectivity curve returns (almost) to the initial value indicating that no major irreversible adsorption to or desorption from the bare gold surface happened. The slight drift seen in the reflectivity values upon potential cycling is attributed to desorption of some contaminants on the Au electrode surface.

Next, the aqueous solution of PEG thiol was introduced into the flow cell, with the potential at the electrode held at $E=0$ V, resulting in a fast self-assembling process to the Au surface followed by quick saturation. After rinsing the system with phosphate buffered saline (PBS) in order to remove any free or loosely bound PEG thiol molecules from the surface and the cell, a potential of $E=-1.1$ V was applied and held constant for 8 min. The reflectivity decreases rapidly to the value of the bare Au. Upon switching the applied potential to $E=0$ V, the reflectivity reaches again the value of bare Au indicating the successful reductive desorption of the PEG thiol SAM from that electrode. The identical adsorption/desorption cycle can be performed several times without any indication of a significant degradation of the Au surface or of the PEG thiol SAM.

For the construction of a sensor array, a gold coated 4-electrode sensor chip was mounted to the combined SPM/SPFM setup and connected to a potentiostat. PEG thiol was allowed to assemble at the whole 4-electrode Au surface. In order to generate the wanted lateral thickness contrast, two of the four electrodes (2nd and 4th from top in Figure 4) were electrochemically treated to remove the PEG monolayer coating. Figure 4(a) shows a series of selected SPM images taken at different angles of incidence, as indicated. One can see that the bare Au

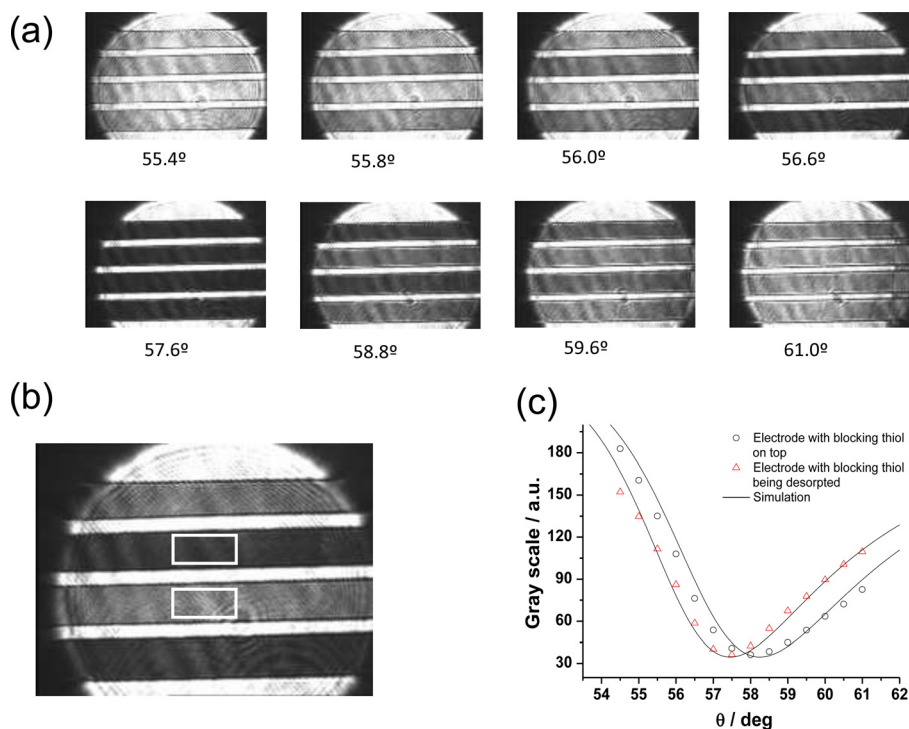


FIG. 4. (a) A series of selected surface-plasmon optical images taken at different incidence angles. Two electrodes (1st and 3rd from top) were covered with PEG thiol SAMs, the other two (2nd and 4th from top) were pure Au (obtained by electrochemical desorption of the monolayer). (b) Representative image with the definition of a pixel field used for the evaluation of a gray value histogram. (c) Average gray values of such pixel frames plotted as a function of the angle at which the respective images were taken, for areas with and without a PEG-thiol monolayer.

electrodes tune into resonance earlier, i.e., at smaller incident angles, while the Au surfaces still covered with a PEG SAMs show the corresponding slight shift of their surface plasmon resonance angle, with the typical contrast inversion²⁸ seen at $\theta \approx 57.6^\circ$. Areas of interests in the images are framed (see Fig. 4(b)), and automatically analyzed by calculating simultaneously the pixel gray value histograms of these frames as a function of the incident angle. The obtained average gray values of the two areas of interest, i.e., with and without PEG thiol, were stored and plotted for both areas (electrodes) as a function of the incidence angle at which the corresponding image was taken (see Fig. 4(c)). The obtained curves agree well with the regular reflectivity curves recorded in the usual Kretschmann configuration and can be quantitatively analyzed in the identical way. The fit curves given in Fig. 4(c) yield a thickness for the PEG thiol layer of $d \approx 4.2$ nm, in agreement with the values derived from the SPR measurements.

V. DESIGNING ADDRESSABLE DNA ARRAYS

For the preparation of an addressable DNA array, the gold coated multi-electrode sensor chip was mounted to the combined SPM and SPFM setup and connected to a potentiostat. The PEG thiol solution in PBS was applied to the sensor chip surface for 20 min in order to allow for the formation of a compact, hydrophilic thiol layer on this 4-electrode system, protecting the surface from unwanted adhesion of molecules introduced during the following processing steps (Fig. 5). In order to start the thiol desorption, one of the electrodes was connected to the potentiostat as working electrode and a constant potential of $E = -1.1$ V was applied for 8 min, followed by a thorough rinse on order to completely remove the PEG thiol producing a fresh, clean gold surface. Biotinylated thiols were then allowed to self-assemble at this bare Au electrode, resulting in a monolayer with a thickness after rinsing of ca. $d = 1.5$ nm (calculated with $n = 1.50$). Next, a streptavidin monolayer of ca. $d = 4.0$ nm in thickness was formed by specific binding from solution to the biotin-sites at the surface. Finally, a layer of biotinylated single-

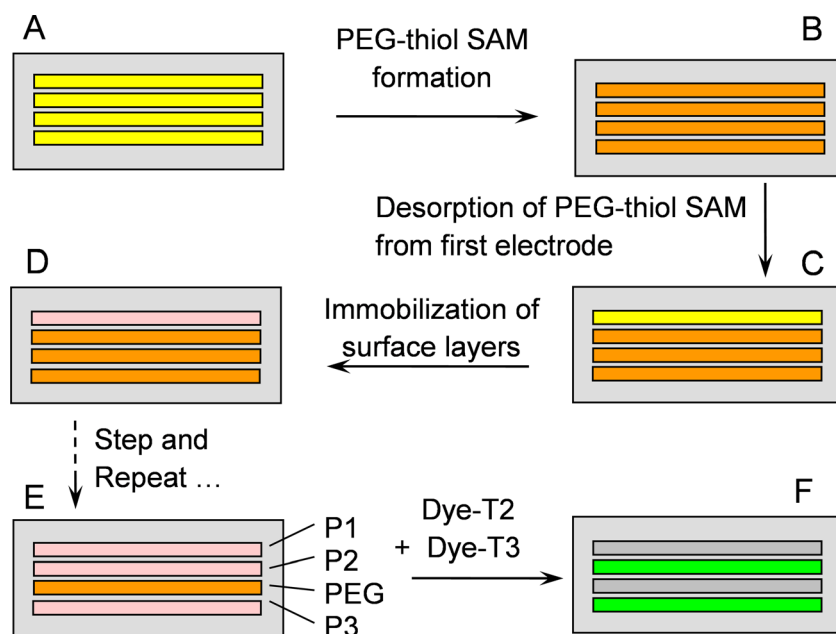


FIG. 5. Schematic steps used for the fabrication of a series of DNA sensor elements on a patterned Au electrode array. Steps of B, C, D, and E are monitored by SPM; step F is recorded by SPFM. First, a PEG thiol solution was incubated on the multi-electrode sensor chip surface to form a compact protecting layer. Then, a constant potential of -1.1 V was applied on one of the electrodes to completely remove the PEG thiol, recovering a fresh, clean gold surface. Biotinylated thiol, streptavidin, and biotinylated single-stranded oligonucleotide solutions were sequentially applied to finally label this electrode with the desired oligo probe. The same procedure was then also applied to the other electrodes, each labeled with a different oligonucleotide probe, while one electrode remained covered with a PEG thiol layer as reference.

stranded oligonucleotide sequences was assembled on the surface by occupying the free binding sites of the streptavidin monolayer.

The same preparation cycles were then applied to the other electrodes until a total of three sensor elements were functionalized, each with a different oligonucleotide capture probe, while one electrode remained covered with a PEG thiol monolayer as reference as it is schematically depicted in Fig. 6. Each interfacial reaction step was characterized by SPR or SPM measurements.

VI. MONITORING PARALLEL DNA HYBRIDIZATION REACTIONS BY SPFM

With the sensor array being oriented relative to the exciting laser beam at an angle near the SPR reflectivity minimum corresponding to the incident angle with the highest surface plasmon field enhancement and thus the highest fluorescence intensities, the target solutions were injected into the flow cell system. Upon hybridization of the targets to the various oligonucleotides capture probe-functionalized Au electrodes, their chromophore tags were excited by the evanescent tail of the propagating surface plasmon waves. The fluorescence photons emitted from the electrode array were then imaged by a color CCD camera.

In a first experiment, the 4-electrode array was prepared with three different capture sequences, P1, P2, and P3, respectively (sequences given in Fig. 6(b)), and one PEG thiol SAM as the inert reference electrode, schematically depicted in Fig. 6(a). The specific 15mer base recognition sequences were separated from the biotin anchor group by 15 thymine nucleotides acting as spacers. Each of the target strands carried a chromophore, Cy5, that could be excited by the red HeNe laser line at $\lambda = 632.8$ nm and emitting fluorescence photons with a peak

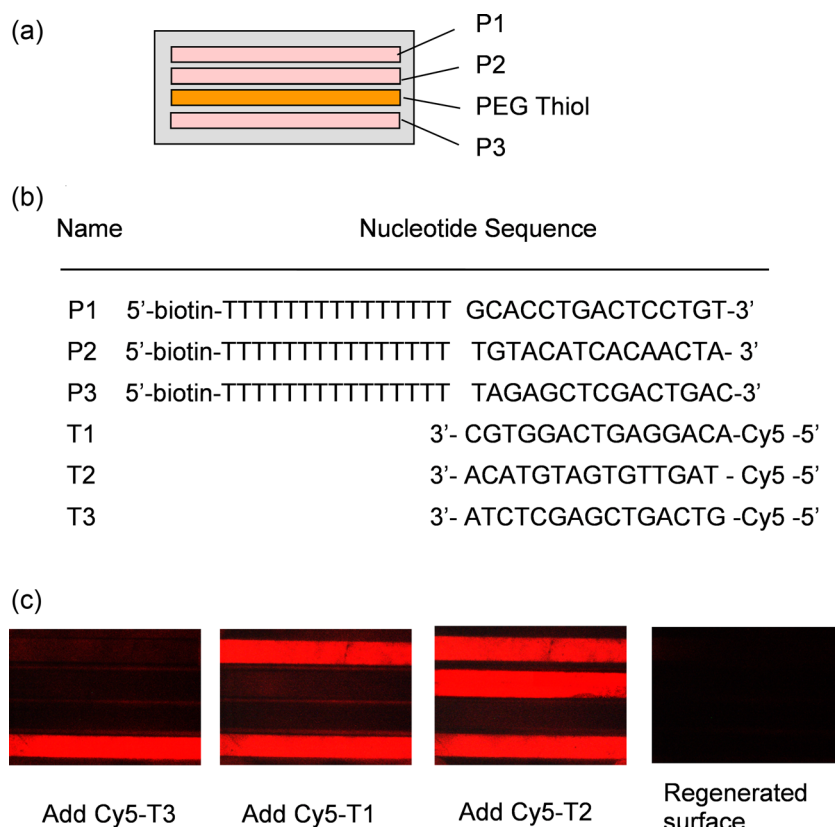


FIG. 6. (a) Schematics of the arrangement of three different probe oligonucleotides and a PEG thiol SAM as reference on a 4-electrode chip. (b) Nucleotide sequences of the probe and target single stranded oligonucleotides used for the experiments. (c) SPFM images showing the electrode selective hybridization following the sequential introduction of the targets T3, T1, and T2, respectively.

intensity at $\lambda = 656$ nm. Injection of 200 nM PBS solutions of each of the three single stranded targets was done sequentially with rinsing steps in between. Figure 6(c) shows the fluorescence microscopic images recorded during this step-after-step addition experiment.

As shown in the first frame of Fig. 6(c), the injection of the target Cy5-T3 resulted in the observation of red fluorescence mostly from stripe P3 according to the high hybridization affinity of this mismatch 0 (MM0) duplex with all other probes being non-complementary. Hence, the other stripes remained almost dark. Subsequently, upon the application of the target Cy5-T1 the red fluorescent could now be observed only from the electrode functionalized with the probe P1 (Fig. 6(c), second frame). And finally, the injection of the target Cy5-T2 led to the decoration of the stripe electrode with the probe P2 (Fig. 6(c), third frame). During the time of these injections and rinsing steps all hybrids were stable and the targets did not dissociate because the k_{off} rate constants for these MM0 duplexes were sufficiently low. Hence, the fluorescence intensities remained constant. However, the surface could be regenerated by rinsing a 10 mM NaOH solution through the flow cell for a few minutes followed by a thorough rinse with pure buffer. This procedure led to the immediate loss of the fluorescence intensity from the bound targets. By this procedure, the probe array could be regenerated for the next test cycle.

In another example for the use of surface plasmon fluorescence microscopy for hybridization studies we present data obtained from experiments with quantum dots (QDs) as fluorescent probes.²⁸ The functionality of the four electrodes (Figure 7(a)) was chosen as follows: the top one was covered by the PEG-thiol passivated SAM, acting as a negative control. The other three electrodes were, from the bottom, functionalized with P1, P2, and a mixture of P1 and P2, respectively (the sequences given in Fig. 7(b)). The target sequence T1 conjugated with

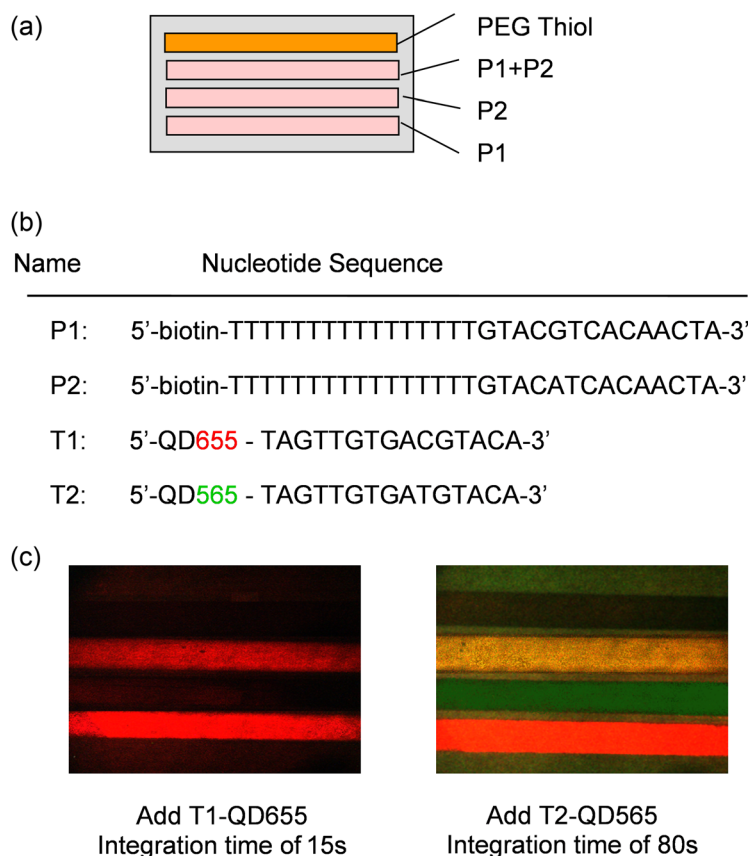


FIG. 7. (a) Schematic arrangement of the probe oligos on a 4-electrode chip for hybridization studies with target oligos being labeled with quantum dots. (b) Nucleotide sequences of the probe and target single stranded DNAs. (c) SPFM images showing the sequential hybridizations following the sequential introduction of T1 and T2.

quantum dots emitting at $\lambda = 655$ nm (T1'-QD₆₅₅ with a red color) and the targets T2, coupled to quantum dots with an emission wavelength of $\lambda = 565$ nm (T2'-QD₅₆₅ emitting in the green) could both be excited with a green HeNe laser at $\lambda = 543$ nm as the light source, using Cr/Ag/Au (2 nm/30 nm/7 nm) as a multi-layer metal film thermally evaporated via a mask onto the glass slide for the preparation of the 4-electrode array.

The final DNA hybridizing experiment presented here was initiated by injecting first a $c_0 = 200$ nM solution of the red-emitting T1'-QD₆₅₅ target sample in PBS. Fig. 7(c) shows the results: the red fluorescence is seen on the electrodes that are functionalized with probe strand P1, either in a single-component SAM or in a mixture with P2 (Fig. 7(c), left frame). The other two electrodes covered by a layer of the P2 probe DNA or by the PEG-thiol SAM remained dark at the employed target concentration of $c_0 = 200$ nM. Subsequently, the T2'-QD₅₆₅ solution was applied to the system and allowed to hybridize to the surface for some time. From Fig. 7(c) right frame, now the green fluorescence of the QD₅₆₅ could be observed from the electrode that was exclusively P2-functionalized. The electrode containing a mixture of P1 and P2, however, changed its color from red to yellow due to the red-green-blue (RGB) color addition of the green fluorescence originating from T2'-QD₅₆₅ with the red fluorescence from the targets T1'-QD₆₅₅. Only the electrode protected with the PEG-thiol again did not show any fluorescence signal.

VII. INTEGRATION OF GRATING-COUPLED SURFACE PLASMON RESONANCE WITH MICROFLUIDICS

In the grating-coupled mode of surface plasmon resonance spectroscopy, a shallow periodic surface corrugation, a grating profile, allows for momentum matching between the incident light and the surface plasmon polaritons. This offers a major advantage of easy integration with other system components, such as microfluidic channels. Figure 8 illustrates one way to realize this kind of integration.

First, a grating profile was fabricated by combining a holographic method for the grating structure²⁹ and photolithography for the channel patterning. Briefly, a HeCd laser beam with a wavelength of $\lambda = 325$ nm passes through a spatial filter to form an expanded collimated beam. This beam is incident on a sample-mirror arrangement so that half of the beam illuminates the sample directly and the other half falls onto the mirror. The mirror then reflects the light so that the reflected light overlaps with the area on the sample directly illuminated by the laser beam, generating an interference pattern. The spatial periodicity of the interference pattern can be controlled by varying the angle between the mirror and the sample.

For the stamp fabrication a cleaned silicon chip used as substrate was first hydrophobized with Hexamethyldisilazane, then a photoresist mixed with a thinner was spin-coated onto the chip. The grating profile with the grating constant of $\lambda = 500$ nm was prepared onto the photoresist surface by the laser holographic method described above. After post baking the sample at 120 °C for 20 min, the holographic grating on the photo resist was transferred into the silicon wafer by reactive ion etching (RIE), using CHF₃/Ar as the process gas. Photoresist residues were removed by acetone. Figure 9 gives an AFM image of such an etched grating profile.

For the micro-channel preparation (cf. Fig. 8(a)), another photoresist layer was spin-coated onto this grating substrate, followed by UV light of $\lambda = 365$ nm (7 mW/cm²) illumination through a mask. After a developing step, a reverse microchannel pattern with a thickness of 7.5 μ m was obtained in the photoresist. After deep reactive ion etching in CF₄ and SF₆, the patterned reverse micro-channels were transferred to the silicon chip. A structure with grating profile on the micro-fluidic channel was thus obtained, which was then used as a positive mold/stamp.

As shown in Figure 8(b), a polymer sensor chip was then fabricated by utilizing a micro-contact stamping process. The patterned silicon stamp was first cleaned and the stamp coated with 150 nm Au by thermal evaporation.

For the final chips with the micro-channel structures polyethylene-co acrylic acid (PEAA) beads were heated on a glass substrate at 90 °C until they were completely molten and then

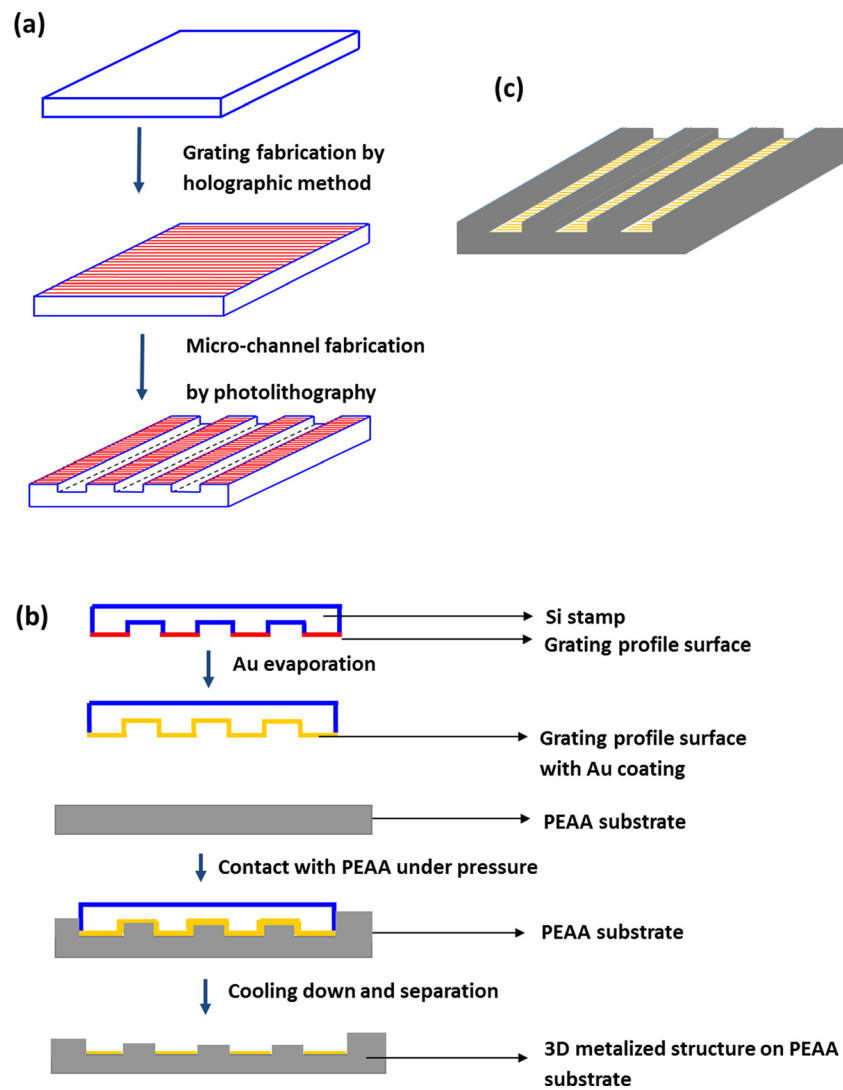


FIG. 8. Schematic representation of (a) the stamp fabrication process and (b) the micro-stamping process; (c) polymer sensor chip combined with micro-channels.

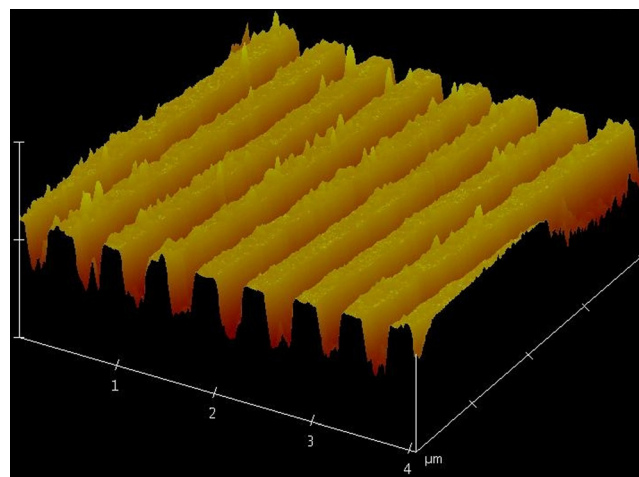


FIG. 9. AFM image of the grating profile etched into the Si stamp.

contacted with the gold coated Si stamp. By applying pressure, the molten PEAA was easily imprinted. The Si stamp and the PEAA were separated after being cooled to room temperature, with the Au coating from the stamp adhering to the plastic substrate, thus being transferred during the stamping process. The schematic drawing of the resulting polymer sensor chip is shown in Figure 8(c). PEAA was chosen as the polymeric substrate because of its good adhesion properties to the metal, compared with other polymers, such as poly (methyl methacrylate), polystyrene, or polycarbonate.

By micro-contact stamping using the pre-fabricated and metal-coated stamp, the micro-channels, the grating profiles, and the evaporated metal could be transferred to the polymeric substrate in one step. The stamped Au adhered well to the substrate, and it was found that the patterns remained stable for over a month after immersion in the PBS solution at pH of 7.4.

SPR data recorded in the angular scan mode before and after the absorption of a monolayer of thiolated poly(ethylene glycol) onto the sensor chip using the metal grating within the micro-channel as the plasmon coupler are shown in Figure 10(a). The SPR was detected using a HeNe laser with $\lambda = 632.8$ nm. A kinetic scan taken during the adsorption process (Fig. 10(b)) demonstrates that this way surface-plasmon based optical sensor formats with gratings as plasmon couplers can be highly integrated with micro-fluidic devices.³⁰

VIII. LOCALIZED SURFACE PLASMONS FOR INTEGRATION INTO MICROFLUIDIC DEVICES

In the recent two decades, localized SPR (LSPR), resulting from a coherent oscillation of the conduction electrons in nanostructured noble metals with light excitation, is broadly used

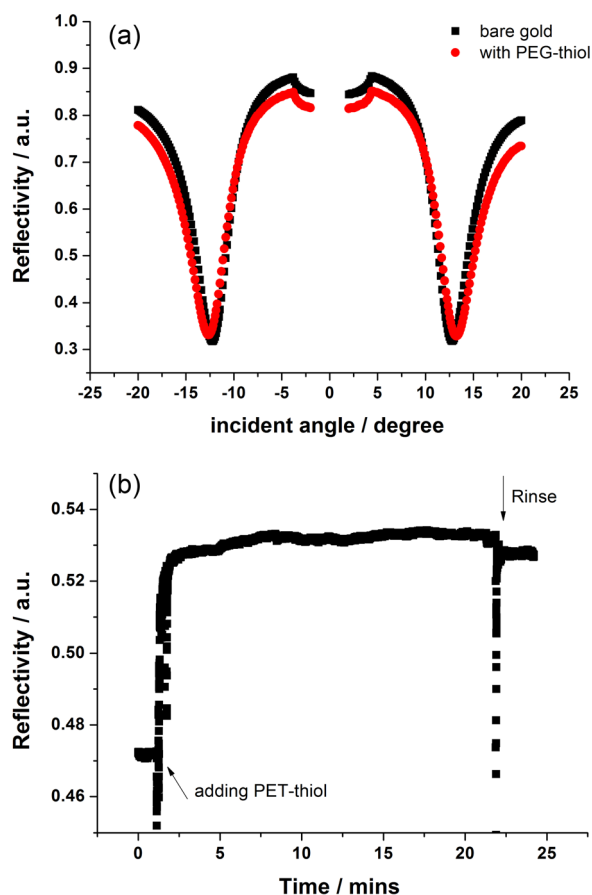


FIG. 10. (a) SPR angular scan before and after PEG thiol adsorption. (b) SPR kinetic scan during the self-assembly of PEG thiol on the Au surface.

for refractive index variation based biosensors.^{31–33} The interest in and the success of LSPR technology is based on state-of-the-art advances in nanofabrication, nanocharacterization, and MEMS fabrication, and is fueled by an increasing demands on lab-on-a-chip and point-of-care systems.

Real-time LSPR has similar features as SPR for interface analyses. The electromagnetic field of the LSPR concentrates within a range of 5–15 nm off the surface of the nanostructure. Although for the detection of bulk refractive index changes, LSPR has a sensitivity of only 10^2 /RIU compared with 10^5 /RIU for SPR, it has a 10 times higher sensitivity for the detection of binding event for viruses, single layers of molecule, e.g., short chain DNA or alkanethiols, with the analytes being in the vicinity of the nanostructures. The shape and the peak wavelength of the LSPR spectra are tunable according to the size, shape and inter-particle distance of the metal nanostructures. Most importantly, the generation of SPR needs a prism, or a grating, or a waveguide to enhance the momentum of the light. But localized surface plasmons can easily be excited whenever the light shines on the nanostructures, and it can be fabricated into a microfluidic device, a sensing array, or a point-of-care system in a cost-effective way.

A. Nanosphere lithography for nanostructure fabrication

Although single metal nanoparticle LSPR has been heavily investigated and demonstrated with the detection of biological samples, a large number of nanostructured particles with identical shape and even distribution on an area larger than $10 \times 10 \mu\text{m}^2$ are desirable for a LSPR chip preparation. In addition, the fabrication of the nanostructures needs to be cost-effective, should allow for the generation of sharp corners and edges in order to enhance the plasmonic signal, and can be fine-tuned to control the excitation peaks of the metal nanostructures.

A range of different nanostructures has been fabricated by nanosphere lithography (NSL): from gold nanocrescents,^{34,35} gold nanoholes with vertical sidewalls,³⁶ to silver nano-triangles,³¹ and gold nanocaps on silica nanospheres.³⁷ We present here nanostructures fabricated by NSL, including 3D nanostructures obtained by oblique evaporating of noble metals on dispersed nanospheres. These structures can be directly used for LSPR detection. The 3D nanostructures in Figure 11(a) show a polarization-dependent excitation as shown in Fig. 11(b), whereas the LSPR spectrum given in Fig. 11(c) was taken with unpolarized light and is the superposition of

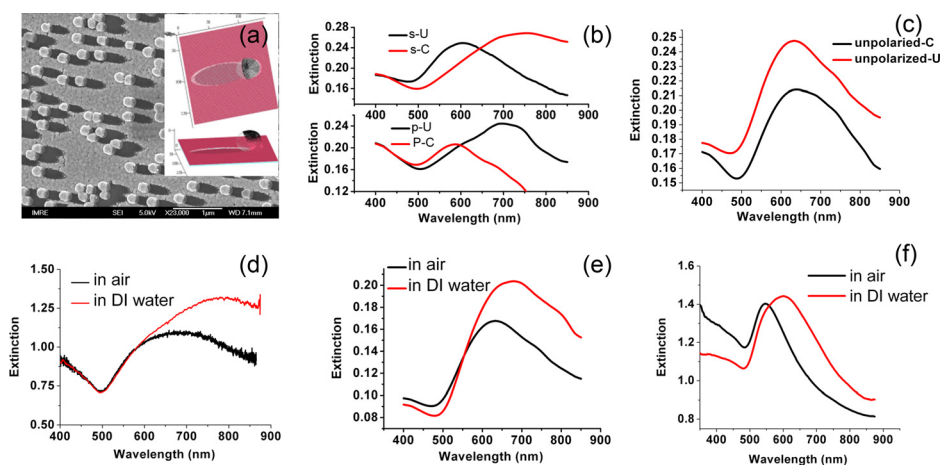


FIG. 11. (a) 3D gold nanostructures fabricated by evaporating 30 nm of gold at 70° onto 170 nm diameter polystyrene nanospheres. The LSPR spectra in (b) indicate these nanostructures are polarization dependent; the spectra in (c) are measured with unpolarized light. U denotes the shadows of gold nanostructures are vertical; C denotes the shadows are horizontal; p is with vertical electrical field; and s is with horizontal electrical field. (d)–(f) The LSPR spectra in air and water, respectively, for various gold nanostructures. The spectra presented in (d) are obtained with nanostructures prepared by evaporating 50 nm of gold onto 170 nm diameter polystyrene nanospheres at 70° ; in (e) with 30 nm of gold; the spectra in (f) were obtained after the nanospheres in (e) were removed. The LSPR sensitivities for (d)–(f) are, respectively, 317, 242, and 170 nm/RIU, RIU is the refractive index unit.

the spectra recorded at orthogonal polarizations. Unpolarized light can be easily used for LSPR sensing, but polarized light can tune the extinction peak of LSPR up to hundreds of nanometers. It was also found that the LSPR sensitivity is dependent on the gold thickness and the existence of the polystyrene nanospheres, as demonstrated in Figs. 11(d)–11(f). If the evaporated gold layer is thinner or the nanospheres are removed, the nanostructures show a lower LSPR sensitivity and narrower bandwidth. Narrow LSPR spectra are preferred, as they give clearer identification of small LSPR spectral shifts and provide a higher signal to noise ratio in LSPR detections.

Nanoholes were fabricated by dispersing 110-nm-diameter polystyrene nanospheres on a $2\text{ cm} \times 2\text{ cm}$ glass substrate,³⁸ evaporating 40 nm of gold film onto the nanospheres, and removing the nanospheres by sonication in water for 40 s. The SEM and AFM images of the fabricated nanoholes are shown in Figs. 12(a) and 12(b). These nanoholes' cross section is not a square but shows a slope, due to the non-conformal gold evaporation in a thermal evaporator, where the capillary force attracted gold atoms to deposit under the nanospheres. Such a profile is different from previously reported nanoholes,^{39,40} however, it benefits from the attachment of more biomolecules in the plasmonic enhanced area.

As an example for the use of these nanostructures for biosensing we studied a biotin-streptavidin (SA) based immunoassay in several steps, with the LSPR spectra taken after each step in air. The result is given in Figures 12(c) and 12(d), respectively. The nanohole sample modified with biotin had a LSPR peak at $\lambda = 567\text{ nm}$. After incubation in streptavidin, the LSPR peak red-shifted by $\Delta\lambda = 11\text{ nm}$. The repeated rinsing by ethanol, PBS, and de-ionized (DI) water blue-shifted the wavelength by 3 nm, because some non-specifically adsorbed molecules were washed away. This LSPR peak shift was mainly coming from streptavidin molecules bound at the circumference of the nanoholes. Based on the size/shape of the nanohole and the streptavidin molecules, we estimate to samples about 218 SA at each nanohole. With a density of the nanoholes being about $3/\mu\text{m}^2$, and the area for detection being 5 mm in diameter defined by the spot size of the illumination light, the effective number of streptavidin molecules monitored per sample is about 1.28×10^{10} , i.e., 21.3 fMol/sample. This is about 3 times of the limit of detection (LOD) reachable by silver nanotriangles measured in a nitrogen gas environment,

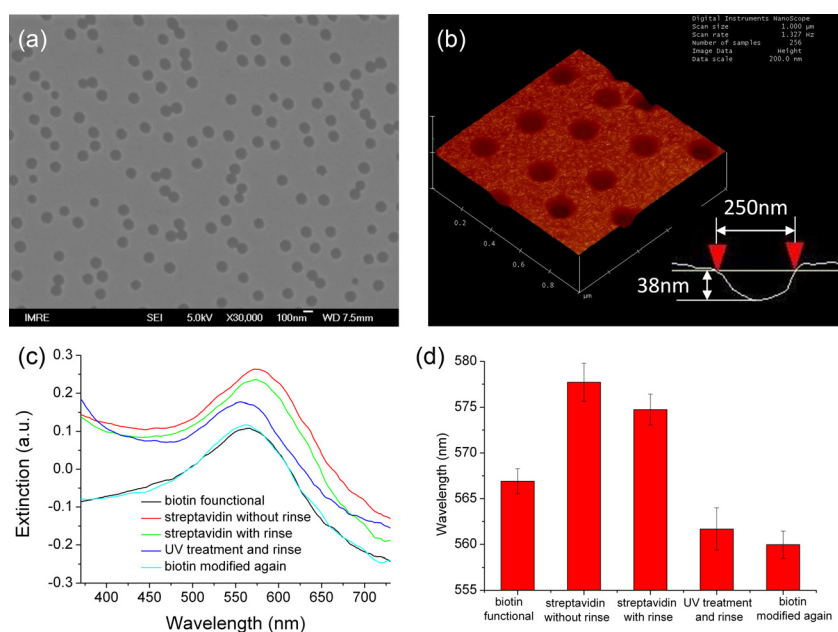


FIG. 12. (a) SEM and (b) AFM images of 40 nm thick gold nanoholes with 110 nm diameter. (c) and (d) present the biotin-streptavidin immunoassay measured by the nanoholes, where (c) shows the extinction spectra of the fabricated gold nanoholes with different surface modifications and (d) shows the error bars for the LSPR peaks at different locations of the sample.

where 4.6×10^9 SA/sample, equivalent to 7.6 fMol/sample, was reported.³¹ However, silver has a much higher LSPR sensitivity, and it will be oxidized easily in air. As also demonstrated in Fig. 12(d) (after UV exposure and rinse), the LSPR peak turned to 561.7 nm, which means the sample is reusable, thus the cost of the device can be further reduced.

B. LSPR and microfluidics

For test purposes, we fabricate a LSPR MEMS device based on a glass-silicon-glass sandwich structure, which is biocompatible due to the long-term stability of glass and silicon compared with other, polymer based MEMS devices. The plasmon-active nanostructures were either nanopillars or nanoholes.

As illustrated in Fig. 13, on the bottom glass substrate, gold nanostructures for LSPR excitation were fabricated by NSL, with a light blocker layer to allow the light to pass only through the gold nanostructures. The middle silicon layer is etched through to form the microfluidics channel and chamber of the device. The top glass holes were drilled as inlet and outlet of the microfluidics. The three layers are bonded together by UV curable epoxy glue. The size of the device was $20 \text{ mm} \times 10 \text{ mm} \times 1.5 \text{ mm}$. Since the whole process avoids high temperature and high pressure, it is nanofabrication compatible. Because the glass surface was not damaged during the process, and the light blocker layer reduced the background of the light, the device is highly transparent with a high signal-to-noise ratio (SNR). As the MEMS fabrication for these three layers are all prepared in wafer level prior to the epoxy bonding, the device is suitable for mass production at low cost.

The integration of this uniform and mass-fabricated gold nanostructure sensor chip into a conventional fluorescent microscope for highly sensitive and facile fluorescent biomarker detection is given in Figure 14. As illustrated in the bottom right inset, a sandwich immunoassay, e.g., capture anti-prostate specific antigen (PSA) antibody (cAb)/PSA/biotinylated detection anti-PSA antibody (biotin-dAb)/streptavidin conjugated QD, was established on the newly developed gold nanopillar or nanohole array fabricated on a glass substrate. The QD was excited by plasmon generated by a gold nanopillar/nanohole array (diameter of 140 nm, and pitch of 400 nm) fabricated by nanoimprinting, and both the fluorescent image of the chip and the emission spectrum from an optical slit were recorded for each PSA concentration. Compared to organic fluorescence dyes, QD provides a brighter signal, prolonged lifetime, and broader Stokes shift. Our study demonstrated that the QD-655 in the PSA bioassay can be excited by LSPR at the wavelength of 540 nm with an emission peak at 655 nm, and the intensity of QD emission signal is proportional to the concentration of PSA, as measured by a microscope with a white light source and a short integration time of 20–100 ms. The fluorescence image recorded by the microscope camera on a gold nanopillar chip can discern PSA at 5 ng ml^{-1} by the naked eye, and the QD emission spectra taken by the microscope with 100 ms of signal integration indicated a LOD below 10 pg ml^{-1} for PSA. Considering the medical screening cut-off of PSA for prostate cancer at 4 ng ml^{-1} , our sandwich bioassay on

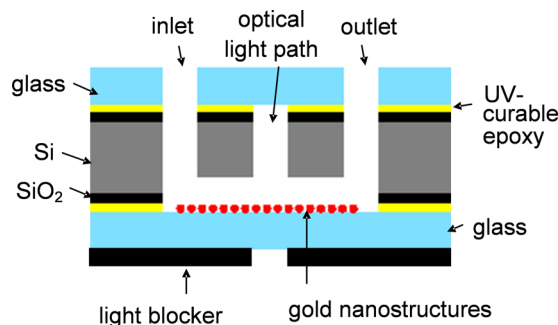


FIG. 13. The cross-section view of the fabricated microfluidic LSPR biosensor.

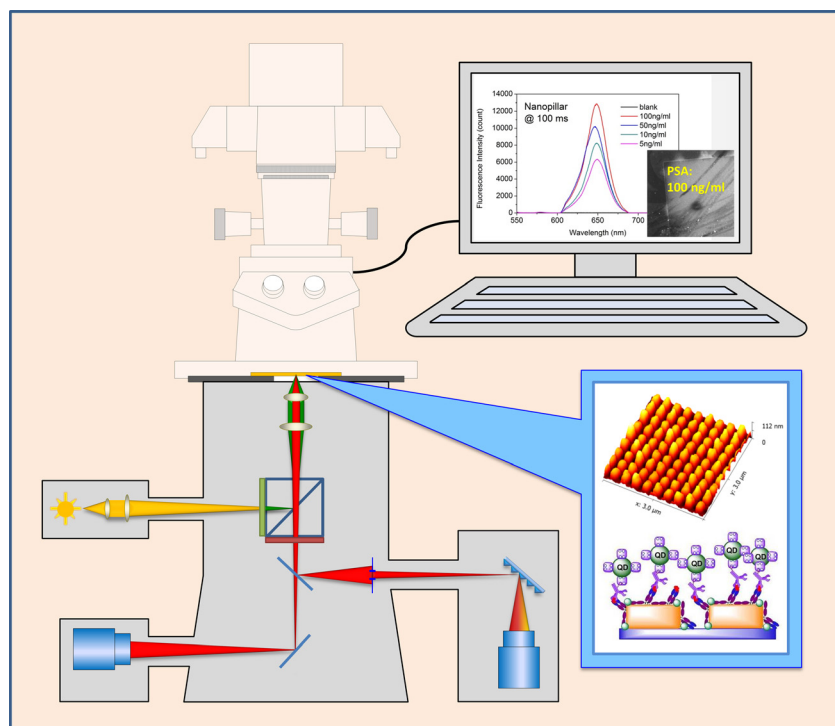


FIG. 14. Schematic representation of an immunodetection setup using a commercial microscope and an LSPR chip with quantum dot (QD) fluorescence enhancement. The computer screen shows the QD emission spectra (PSA at different concentrations) and the dark-field image of the sensor chip (PSA, 100 ng ml⁻¹, 100 ms integration time); bottom right inset shows the schematic illustration of QD-655 sandwich immunoassay and the AFM image of the sensor chip (gold nanopillar array, 100 ng ml⁻¹ of PSA).

the nanostructured sensing chip has great potential to be used in a miniaturized point-of-care system for PSA early stage diagnosis.

IX. CONCLUSION

This paper demonstrated several strategies of integrating a plasmonic biosensing chip with microfluidics. While plasmons can be generated by gold film, grating-coupled SPR, or gold nanostructure based LSPR, and plasmons can be used for biomolecular detection via the angle shift in SPR, wavelength shift in LSPR, or fluorescent dyes excited by SPR or LSPR, our work gave some details in these different strategies, including the cost-effective chip and microfluidic fabrication, the bioassay design and surface functionalization, and the detection methods.

For the fluorescent dyes excited by SPR, a 4-element SPR array was fabricated by gold evaporation and electrochemical assisted surface functionalization control, and the microfluidics used was a micro-machined flow cell. Such a device could well detect the hybridization of three different DNA targets. For the SPR for angle interrogation, grating was fabricated by holographic method and the microfluidics was fabricated on the same chip by photolithography and silicon etching, and the microfluidic chip could detect the absorption of a monolayer of thiolated PEG. For the gold nanostructure based LSPR chips, the nanoholes were fabricated by nanosphere lithography, the nanohole chip was integrated with microfluidic device in glass-silicon-glass sandwich layer, and the device could detect the streptavidin at 21.3 fM/sample by the LSPR wavelength shift. Finally, we fabricated gold nanopillar and nanohole arrays by nanoimprinting, and the plasmonic array in microfluidics showed a LOD below 10 pg ml⁻¹ for PSA detection via a sandwich assay with QDs excited by LSPR.

With the advancement of nanotechnologies, microfluidics, and portable instrumentation systems, we predict that an ideal plasmonic integrated microfluidics will become more compact,

more sensitive, even low-cost, and will be in a multiplexed format for diagnostics. In this paper, we have proven that plasmonic integrated microfluidics is a wide application tool for various biomolecule detections, and the design and fabrication of the device is based on application. We believe the summary of our work will shed some light on different strategies towards an ideal plasmonic device for point-of-care diagnostics.

ACKNOWLEDGEMENTS

The fabrication and characterization of the sensing chips were conducted in SERC nano fabrication, processing and characterisation (SnFPC) at the Institute of Materials Research and Engineering (IMRE), A*STAR, and the authors are indebted to the kind help of the staff in SFNC.

- ¹S. Lofas, B. Johnson, K. Tegendal, and L. Roenuberg, "Dextran modified gold surfaces for surface plasmon resonance sensors: Immunoreactivity of immobilized antibodies and antibody-surface interaction studies," *Colloids Surf., B* **1**, 83–89 (1993).
- ²O. Tokel, F. Inci, and U. Demirci, "Advances in plasmonic technologies for point of care applications," *Chem. Rev.* **114**, 5728–5752 (2014).
- ³A. G. Brolo, "Plasmonics for future biosensors," *Nat. Photonics* **6**, 709–713 (2012).
- ⁴J. Kim, "Joining plasmonics with microfluidics: From convenience to inevitability," *Lab Chip* **12**, 3611–3623 (2012).
- ⁵C. Escobedoab, "On-chip nanohole array based sensing: A review," *Lab Chip* **13**, 2445–2463 (2013).
- ⁶W. Knoll, "Interfaces and thin films as seen by bound electromagnetic waves," *Annu. Rev. Phys. Chem.* **49**, 569–638 (1998).
- ⁷J. G. Gordon and J. D. Swalen, "The effect of thin organic films on the surface plasma resonance on gold," *Opt. Commun.* **22**, 374–376 (1977).
- ⁸D. Casper, M. Bukhtiyarova, and E. B. Springman, "A Biacore biosensor method for detailed kinetic binding analysis of small molecule inhibitors of p38 alpha mitogen-activated protein kinase," *Anal. Biochem.* **325**(1), 126–136 (2004).
- ⁹B. Rothenhäusler and W. Knoll, "Surface-plasmon microscopy," *Nature* **332**, 615–617 (1988).
- ¹⁰W. Knoll, M. Liley, D. Piscevic, J. Spinke, and M. J. Tarlov, "Supramolecular architectures for the functionalization of solid surfaces," *Adv. Biophys.* **34**, 231–251 (1997).
- ¹¹T. Liebermann and W. Knoll, "Surface-plasmon field-enhanced fluorescence spectroscopy," *Colloids Surf., A* **171**(1–3), 115–130 (2000).
- ¹²F. Yu, B. Persson, S. Lofas, and W. Knoll, "Atto-molar sensitivity of surface plasmon fluorescence spectroscopy," *J. Am. Chem. Soc.* **126**, 8902–8903 (2004).
- ¹³T. Liebermann and W. Knoll, "Parallel multispot detection of target hybridization to surface-bound probe oligonucleotides of different base mismatch by surface-plasmon field-enhanced fluorescence microscopy," *Langmuir* **19**, 1567–1572 (2003).
- ¹⁴S. Meltzer and D. Mandler, "Microwriting of gold patterns with the scanning electrochemical microscope," *J. Electrochem. Soc.* **142**(6), L82–L84 (1995).
- ¹⁵V. Romanov, S. N. Davidoff, A. R. Miles, D. W. Grainger, B. K. Gale, and B. D. Brooks, "A critical comparison of protein microarray fabrication technologies," *Analyst* **139**(6), 1303–2612 (2014).
- ¹⁶N. L. Abbott, J. P. Folkers, and G. M. Whitesides, "Manipulation of the wettability of surfaces on the 0.1-micrometer to 1-micrometer scale through micromachining and molecular self-assembly," *Science* **257**(5075), 1380–1382 (1992).
- ¹⁷M. M. Walczak, D. D. Popenoe, R. S. Deinhammer, B. D. Lamp, C. K. Chung, and M. D. Porter, "Reductive desorption of alkanethiolate monolayers at gold—A measure of surface coverage," *Langmuir* **7**(11), 2687–2693 (1991).
- ¹⁸S. Imabayashi, D. Hobara, T. Kakiuchi, and W. Knoll, "Selective replacement of adsorbed alkanethiols in phase-separated binary self-assembled monolayers by electrochemical partial desorption," *Langmuir* **13**(17), 4502–4504 (1997).
- ¹⁹C. B. Ross, L. Sun, and R. M. Crooks, "Scanning probe lithography. 1. Scanning tunneling microscope induced lithography of self-assembled N-alkanethiol monolayer resists," *Langmuir* **9**(3), 632–636 (1993).
- ²⁰L. M. Tender, R. L. Worley, H. Y. Fan, and G. P. Lopez, "Electrochemical patterning of self-assembled monolayers onto microscopic arrays of gold electrodes fabricated by laser ablation," *Langmuir* **12**(23), 5515–5518 (1996).
- ²¹T. G. Drummond, M. G. Hill, and J. K. Barton, "Electron transfer rates in DNA films as a function of tether length," *J. Am. Chem. Soc.* **126**(46), 15010–15011 (2004).
- ²²T. G. Drummond, M. G. Hill, and J. K. Barton, "Electrochemical DNA sensors," *Nat. Biotechnol.* **21**(10), 1192–1199 (2003).
- ²³W. Hickel and W. Knoll, "Surface plasmon microscopy of lipid layers," *Thin Solid Films* **187**(2), 349–356 (1990).
- ²⁴W. Hickel, D. Kamp, and W. Knoll, "Surface-plasmon microscopy," *Nature* **339**, 186–186 (1989).
- ²⁵K. L. Prime and G. M. Whitesides, "Adsorption of proteins onto surfaces containing end-attached oligo(ethylene oxide): A model system using self-assembled monolayers," *J. Am. Chem. Soc.* **115**, 10714–10721 (1993).
- ²⁶S. I. Jeon, J. H. Lee, J. D. Andrade, and P. G. De Gennes, "Protein-surface interactions in the presence of polyethylene oxide: I. Simplified theory," *J. Colloid Interface Sci.* **142**(1), 149–158 (1991).
- ²⁷R. Kötz, D. M. Kolb, and J. K. Sass, "Electron density effects in surface plasmon excitation on silver and gold electrodes," *Surf. Sci.* **69**, 359–364 (1977).
- ²⁸L. Niu and W. Knoll, "Electrochemically addressable functionalization and parallel read-out of a DNA biosensor array," *Anal. Chem.* **79**, 2695–2702 (2007).
- ²⁹X. Mai, R. Moshrefzadeh, U. J. Gibson, G. I. Stegeman, and C. T. Seaton, "Simple versatile method for fabricating guided-wave gratings," *Appl. Opt.* **24**, 3155–3161 (1985).

- ³⁰N. Zhang, H. Liu, and W. Knoll, "A disposable polymer sensor chip combined with micro-fluidics and surface plasmon resonance," *Biosens. Bioelectron.* **24**, 1783–1787 (2009).
- ³¹A. J. Haes and R. P. Van Duyne, "A nanoscale optical biosensor: Sensitivity and selectivity of an approach based on the localized surface plasmon resonance spectroscopy of triangular silver nanoparticles," *J. Am. Chem. Soc.* **124**(35), 10596–10604 (2002).
- ³²J. N. Anker, W. P. Hall, O. Lyandres, N. C. Shah, J. Zhao, and R. P. Van Duyne, "Biosensing with plasmonic nanosensors," *Nat. Mater.* **7**, 442–453 (2008).
- ³³B. Sepulveda, P. C. Angelome, L. M. Lechuga, and L. M. Liz-Marzan, "LSPR-based nanobiosensor," *Nano Today* **4**, 244–251 (2009).
- ³⁴Y. Lu, G. L. Liu, J. Kim, Y. X. Mejia, and L. P. Lee, "Nanophotonic crescent moon structures with sharp edge for ultra-sensitive biomolecular detection by local electromagnetic field enhancement effect," *Nano Lett.* **5**, 119–124 (2005).
- ³⁵H. Rochholz, N. Bocchio, and M. Kreiter, "Tuning resonances on crescent-shaped noble-metal nanoparticles," *New J. Phys.* **9**(3), 53 (2007).
- ³⁶J. Prikulis, P. Hanarp, L. Olofsson, D. Sutherland, and M. Käll, "Optical spectroscopy of nanometric holes in thin gold films," *Nano Lett.* **4**(6), 1003–1007 (2004).
- ³⁷T. Endo, K. Kerman, N. Nagatani, H. M. Hiepa, D.-K. Kim, Y. Yonezawa, K. Nakano, and E. Tamiya, "Multiple label-free detection of antigen-antibody reaction using localized surface plasmon resonance-based core-shell structured nanoparticle layer nanochip," *Anal. Chem.* **78**, 6465–6475 (2006).
- ³⁸G. Xiang, N. Zhang, and X. Zhou, "Localized surface plasmon resonance biosensing with large area of gold nanoholes fabricated by nanosphere lithography," *Nanoscale Res. Lett.* **5**, 818–822 (2010).
- ³⁹T. Rindzevicius, Y. Alaverdyan, A. Dahlin, F. Höök, D. S. Sutherland, and M. Käll, "Plasmonic sensing characteristics of single nanometric holes," *Nano Lett.* **5**, 2335–2339 (2005).
- ⁴⁰D. Gao, W. Chen, A. Mulchandani, and J. S. Schultz, "Detection of tumor markers based on extinction spectra of visible light passing through gold nanoholes," *Appl. Phys. Lett.* **90**, 073901 (2007).